Mohanna *et al. Earth, Planets and Space* (2025) 77:130
https://doi.org/10.1186/s40623-025-02197-7

Earth, Planets and Space

EXPRESS LETTER

Open Access

The 2024 Noto earthquake and tsunami: insights from the static and adjoint state inversion methods

Saeed Mohanna[1], Lingsen Meng[1*], Tung-Cheng Ho[2], Chao An[3] and Liuwei Xu[1]

Abstract

In this study, we investigated the coseismic slip and deformation caused by the 2024 M_w 7.5 earthquake on the Noto Peninsula and the subsequent tsunami through both adjoint and static inversion modeling techniques. We leveraged a network of tsunami stations available across the Sea of Japan, along with detailed near-field geodetic data from GNSS stations and SAR-derived 3D deformation, to conduct these inversions. Our analyses generally revealed a significant slip zone northeast of the epicenter, corresponding to a deeper fault plane dipping 70º to the northwest. Notably, our adjoint inversion method successfully identified a landslide source in Toyama Bay, inferred directly from tsunami waveform data. This represents the first time a landslide source has been resolved by inverting water elevation data, highlighting the exceptional capability of the adjoint method in detecting non-seismic tsunami sources. The use of both modeling techniques not only enhanced our understanding of seismic events in this geologically complex region but also demonstrated the critical role of integrated geodetic and water elevation data for improving tsunami modeling and hazard assessment.

Keywords Noto tsunami, Submarine landslide, Tsunami imaging, Adjoint inversion, Static inversion

*Correspondence:
Lingsen Meng
lsmeng@g.ucla.edu
Full list of author information is available at the end of the article

Graphical Abstract

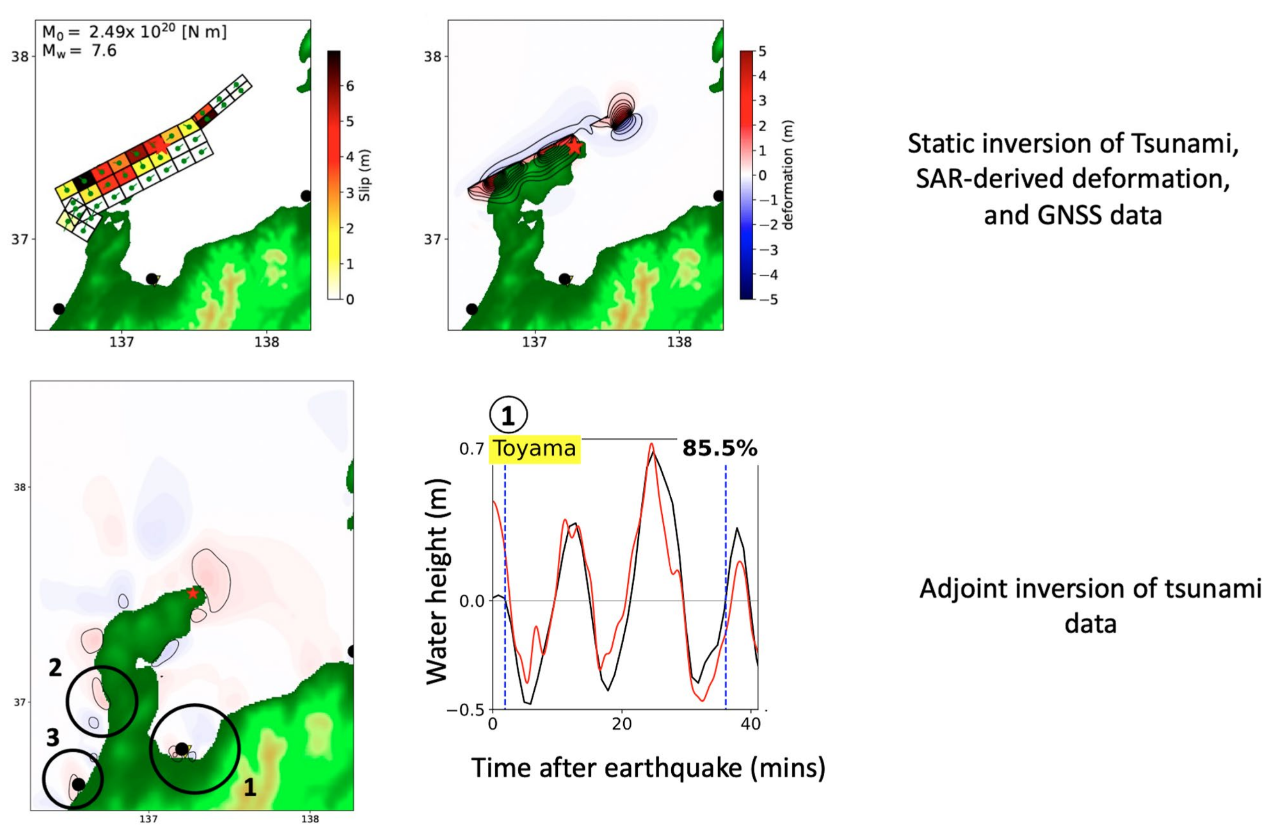

1 Introduction

At 16:10:09 local time on New Year's Day 2024, a magnitude 7.5 earthquake hit the Noto Peninsula in Ishikawa Prefecture, Japan, as reported by the United States Geological Survey (2021). The USGS identified the earthquake as occurring on a northeast–southwest striking reverse fault, with the epicenter located at 37.487°N, 137.271°E (Fig. 1) at a depth of 10 km. Preceding the mainshock, the Japanese Meteorological Agency (JMA) detected two foreshock events with magnitudes of 5.5 and 4.6 occurring approximately 4 and 2 min earlier, respectively. The earthquake initiated an aftershock sequence, with over 6500 events of $M_{JMA} > 2$, extending offshore to the northeast of the peninsula. This sequence was part of a 4-year earthquake swarm that started in late 2020 at depths greater than 15 km, with notable increases in seismicity in 2021, 2022, and 2023. The swarm included a migration of events upward to depths generally between 10 and 15 km, culminating in a series of earthquakes in 2023 that reached M_{JMA} of up to 6.5. Although the region lacks significant volcanic and geothermal activity, researchers have suggested that changes in pore fluid pressure may explain the persistent seismicity (Nishimura et al. 2023; Kato 2024; Amezawa et al. 2023; Yoshida et al. 2023).

The 2024 M_w 7.5 earthquake triggered a tsunami, with a maximum estimated tsunami inundation of ~5.5 m (Yuhi et al. 2024). These cascading disasters resulted in 299 fatalities and 1208 injuries (Ishikawa Prefectural Government 2024). Extensive studies have identified the Sea of Japan, particularly the Ishikawa Prefecture, as being highly susceptible to tsunamis (Satake et al. 2022; Mulia et al. 2020; Woessner and Farahani 2020). Notable previous tsunamis in the eastern Sea of Japan include ones caused by the 1833 M 7.5–7.7 Shonai, 1940 M_w 7.5 Shakotan, 1964 M_w 7.6 Niigata, 1983 M_w 7.8 Akita, and 1993 M_w 7.7 Okushiri earthquakes, which caused fatalities ranging from 10 to 230 and wave run-ups as high as 32 m, with the latter recorded during the 1993 event (National Geophysical Data Center 2024). The 1741 Oshima volcano eruption further exemplifies the region's tsunami potential, having generated run-up heights up to 34 m and resulting in 1467 to 2033 fatalities (Satake 2007; Byun and Kim 2021).

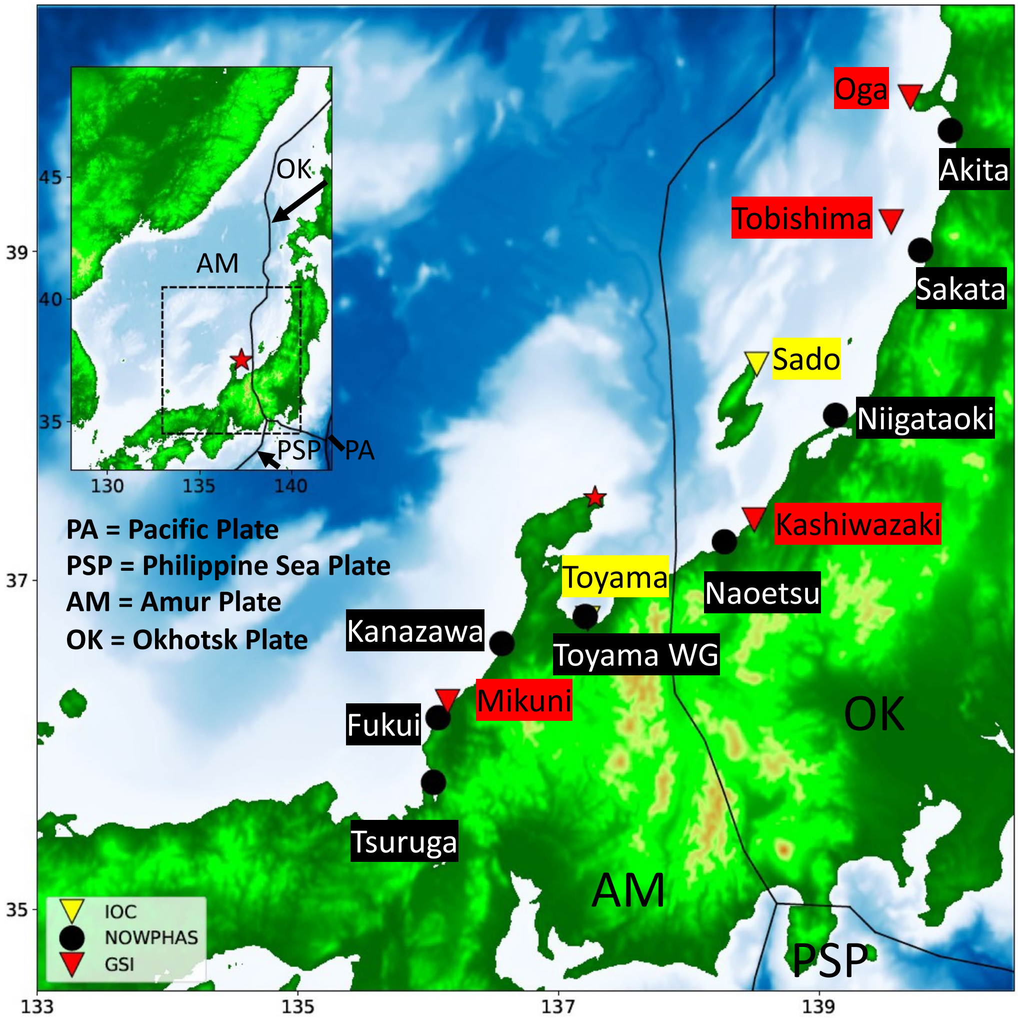

Fig. 1 Overview map. Black lines in the inset and main map show plate boundaries. The dashed black rectangle in the inset shows the main area of study. Plate motions (USGS, n.d.) are also indicated. Names of stations used throughout this study are labeled on the main map. Inverted triangles and black circles show tide and wave gauge locations in the Sea of Japan from various agencies, highlighted by different colors shown in the legend. The red star shows the USGS epicenter of the earthquake. Horizontal and vertical axes show degrees of longitude and latitude, respectively

Research efforts by the Ministry of Land, Infrastructure, Transport, and Tourism (MLIT 2014) and the Japan Sea Earthquake and Tsunami Project (JSPJ—Sato et al. 2020) have provided detailed mappings of offshore faults in the Sea of Japan. Murotani et al. (2022) pinpointed the specific faults responsible for the 1940, 1983, and 1993 earthquakes using waveform and run-up data, highlighting the ongoing seismic risk. Furthermore, Fujii and Satake (2024) have identified offshore faults between Noto and Sado Island that pose a continuing threat. In addition, a forward modeling study by Masuda et al. (2024a) explored various fault model scenarios for this event, suggesting that a landslide in Toyama Bay could explain discrepancies observed at several tsunami stations, thereby corroborating the cascading hazards in this seismic event.

In this study, we utilize data from tsunamis, the Global Navigation Satellite System (GNSS), and Synthetic Aperture Radar (SAR)-derived 3D deformation (see Fig. 1) to estimate coseismic displacement along an assumed fault geometry. In addition, we employ tsunami data to determine the initial water elevation (IWE) directly using the adjoint-state inversion method. No previous studies have attempted to constrain the fault rupture by jointly inverting these three data sets, which can provide better constraints on the coseismic process. Furthermore, the direct retrieval of IWE through the adjoint method offers promising insights into resolving the secondary hazards of this event. Specifically, our approach aims to investigate the coseismic seafloor displacement and assess the potential for landslides triggered within Toyama Bay.

2 Methods

2.1 Static inversion

To model the slip of the 2024 Noto Peninsula earthquake, we performed inversions of tsunami, GNSS, and SAR-derived deformation data using the non-negative least squares method outlined by Lawson and Hanson (1995) with the assumption of instantaneous fault rupture. We refer to this as a static inversion. The assumed fault geometry is derived by coarsening the 469 fault planes from Ma et al. (2024, Fig. S1). The fault model we obtained incorporates a total of 34 subfaults distributed over three fault segments, with segment lengths ranging from 18 to 96 km and widths between 27 and 36 km. The specific parameters for each subfault are detailed in Supplementary File 2. Coarsening was done to streamline the computation of Green's functions (GFs) and to reduce the patchiness in the static inversion's slip model. GFs were generated with assumed rakes of 90 and 180 degrees to invert for the fault slip, targeting rake angles within the range of 135 ± 45 degrees.

To simulate tsunami waveforms, we used the Okada (1985) seafloor deformation model, which provides an analytical solution for surface deformation caused by shear and tensile faults in a homogeneous, elastic half-space, assuming unit slip on each subfault. This deformation field was then forward modeled to the tsunami stations using the Parallel Cornell Multi-grid Coupled Tsunami Model (PCOMCOT) software (Liu et al. 1998; An et al. 2014; Wang and Liu 2006; Zhu et al. 2021).

Our model utilized nested, two-layer bathymetry data: 15-arcsec resolution data from the General Bathymetric Chart of the Oceans (GEBCO) 2023 grid, supplemented with higher resolution 6-arcsec data from the Japan Hydrographic Association, as depicted in Figure S2. To ensure numerical stability and to satisfy the Courant–Friedrichs–Lewy (CFL) condition, we employed a time step of 0.2 s (CFL ~0.1<1). Due to resolution limits in bathymetry, some tsunami station locations provided by respective agencies were positioned on land, necessitating adjustments to the nearest offshore grid point with a depth greater than 0 m to ensure accurate simulation of tsunami wave arrival.

2.2 Adjoint inversion

To directly image the tsunami source, we employed the adjoint-state inversion method. This technique was developed to accurately determine the tsunami source—specifically, the (IWE)—by minimizing the misfit between observed and predicted tsunami waveforms. The method incorporates time-reversal imaging (TRI), a process pioneered by Hossen et al. (2015), which reverses observed tsunami waveforms in time and back-propagates them from station locations, treated as point sources. At the end of the reversed time series, the wavefields constructively interfere at the source location, though the IWE may exhibit amplitude and locational distortions, contingent on station density and azimuthal coverage. This is used as an initial guess in our inversion.

This distorted IWE is then forward modeled to the station locations using PCOMCOT, and the L2 norm misfit functional between the observed and predicted values is computed. This misfit is minimized by attempting to reduce the gradient of the misfit function to zero. Since the gradient with respect to the source parameters is equivalent to the adjoint wavefield (Plessix 2006; Tarantola 1986; Tromp et al. 2004), we back-propagate the data residuals at each station to the original source via TRI. The original IWE is then iteratively refined using the conjugate gradient method until the misfit functional converges, enhancing the accuracy of the tsunami source model.

For further insights into the adjoint method, we direct readers to the detailed discussions in Zhou et al. (2019) and Xie et al. (2023). To expedite the computation process, we utilized 30-arcsec bathymetry data from the GEBCO 2023 grid and conducted 50 iterations of the inversion.

3 Data

Horizontal coseismic offset data were acquired from 21 three-component GNSS stations, which are part of Japan's GNSS Earth Observation Network System (GEONET). These data were processed by the Nevada Geodetic Laboratory (NGL 2024) using the Jet Propulsion Laboratory's GipsyX software (Bertiger et al. 2020), resulting in a time series with a 5-min sampling interval. To remove the impact of the M_w 6.2 aftershock that occurred 8 min following the mainshock, only data collected between the two events were used to calculate the coseismic offset of the mainshock. To determine the station weights in the static inversion, we took the reciprocal of the normalized average error across the horizontal components at each station (Table S1), with the normalization performed relative to the minimum value.

The 3D SAR-derived deformation data were obtained from Ma et al. (2024). These were generated by processing several SAR images from the ALOS-2 and Sentinel-1 satellites into deformation maps for those respective tracks. They are then inverted into 3D deformations (319,074 points per component) using the Strain Model and Variance Component Estimation (SM–VCE) toolbox (Liu et al. 2022). The correlation of their resulting maps with the GNSS stations used in their study was 0.93, suggesting high reliability.

For the tsunami data, we sourced a variety of measurements, including tide (TG), wave gauge (WG), and buoy data from multiple agencies (Fig. 1). We acquired data from 2 tide gauge stations with 1-min sampling intervals from the International Oceanographic Commission (IOC), 4 stations from the Geospatial Information Authority of Japan (GSI) with 30-s intervals, and 8 WG stations, sampled every 30 s, were digitized from the Nationwide Ocean Wave information network for Ports and HArbourS (NOWPHAS) of Japan website.

To mitigate the impact of ocean tides on the tsunami data, we employed a bandpass filter with a range of 240–3600 s for a time series sampled every 1 or 0.5 min. The lower limit was chosen such that high-frequency noise is minimized while still allowing for potential submarine landslide detection (Mulia et al. 2024). For the digitized data from the NOWPHAS, we interpolated the data to a 1 Hz sampling rate before applying the 240–3600 s bandpass filter. The maximum recorded first-arriving tsunami wave amplitude of 0.8 m was at the Naoetsu WG station. The waveform spectra, in addition to the raw and filtered data, can be found in Figs. S3 and S4.

For both inversions, we generally selected the inversion window such that it contained the first complete peak and trough of each station's time series. Optimal tsunami station weights were determined by an iterative weighting technique that seeks to balance waveform fitting with the number of stations used in the inversion. This is achieved by removing stations with exceptionally poor fits until the overall fitting of the data set no longer improves.

In the joint inversion of tsunami, SAR-derived deformation and GNSS data, weights of 0.1, 0.1, and 1.0 were assigned to each data set, respectively, determined by trying different combinations of weights and finding the one yielding the best average fitting across the three data sets. Using the optimal data set weights, we also searched for the optimal smoothness parameter using Akaike's Bayesian Information Criterion (ABIC; Akaike 1980; Sekiguchi et al. 2000). The details and results of the optimizations can be found in Text S1 and Figs. S5–S7 and S25, S26, respectively.

To evaluate the fit between observed and predicted data for both GNSS and tsunami data sets, we employ the variance reduction (VR) metric, a standard measure widely used in tsunami modeling studies (Mizutani et al. 2024; Xie et al. 2023; Kubota et al. 2021). A VR closer to 100% means a perfect fit, while a VR<0% corresponds to a poor fit. The formal definitions we used to measure VR at tsunami, SAR, and GNSS observations ($VR_{tsunami}$, VR_{SAR}, and VR_{GNSS}) can be found in Text S2.

Our checkerboard tests (Figures S8, S9) show a generally successful reproduction of the synthetic slip model. The best resolution is found on the shallower part of the central fault segment in the case of a joint inversion, and the least resolved patches are in the deeper part of the central fault segment. Fitting in these cases yielded VR≥ 95% for all data sets. Using only SAR-derived deformation data also yielded similarly high VR values and even better slip model resolution. This may be due to the high spatial density of SAR-derived deformation data being applied to a coarse fault geometry, resulting in an overdetermined inverse problem. In addition, the central fault segment parameters were partly constrained by fitting the deformation data (Ma et al. 2024). When we add Gaussian noise to the synthetic checkerboard data, the resulting test (Fig. S9c) shows that the onshore subfaults, where SAR observations are concentrated, are better resolved than the offshore ones. The GNSS- and tsunami-only tests achieved poorer slip resolutions.

4 Results

4.1 Static inversion

Our static inversion results, integrating tsunami, SAR-derived deformation, and GNSS data, indicate slip values of up to 7 m and a peak vertical crustal deformation of ~3.9 m above the central fault segment (Fig. 2a). The slip distribution across the fault segments highlights peak slip occurrences on the western part of the central fault segment. The westernmost segment had a peak slip value of 0.6 m, and the offshore segment had a peak value of 6.6 m. With an assumed rigidity of 30 GPa, we estimated the seismic moment to be 2.9×10^{20} N m, corresponding to a moment magnitude (M_w) of 7.6. Our results using other combinations of data sets (Figures S10–S17; Tsunami+SAR, Tsunami+GNSS, SAR+GNSS, Tsunami-only, SAR-only and GNSS-only) obtained peak slip values ranging between 0.5 and 40 m, with M_w ranging between 7.1 and 7.9. These estimates are slightly wider in range than values reported by other researchers, with M_w ranging between 7.4 and 7.7 (Fujii and Satake 2024; Mizutani et al. 2024) and figures of 7.5 from JMA and USGS. All these additionally obtained fault ruptures lead to peak vertical crustal deformations ranging between 0.35 and 12 m, usually located on the central fault segment. In the Fujii and Satake (2024) study, the peak slip value in the joint inversion was located offshore. The USGS and Mizutani et al. (2024) results had peak slip values on the central fault segment. Although our study's peak slip was on the central segment, we also obtained significant slip on our offshore fault plane (up to ~6 m). Detailed slip and rake values for each subfault are documented in Supplementary File 2.

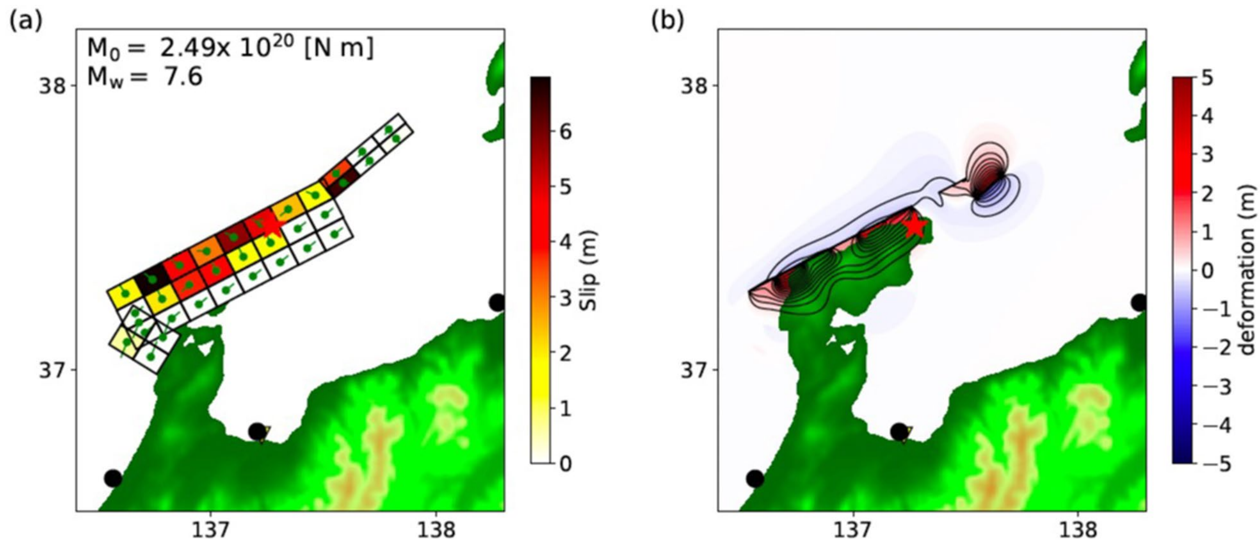

Fig. 2 Results of our joint static inversion of Tsunami, SAR-derived deformation, and GNSS data sets. **a** Our obtained fault slips. Rake directions are indicated by the green arrows. **b** Calculated vertical deformation from the Okada (1985) model of the fault slips from (**a**). Deformation is shown in intervals of 0.25 m

For coseismic displacements at GNSS stations (Fig. 3a), we obtained an overall VR_{GNSS} of ~ 13%. While the overall VR_{GNSS} may be low, the VR of the amplitudes ($VR_{GNSS,amp}$) and phase ($VR_{GNSS,pha}$) are significantly higher, at 64 and 96%, respectively. The fitting in Fig. 3a indicates that the fits in the east–west component are better than those in the north–south component. A similar pattern is also seen in the SAR-derived deformation fitting (Fig. 3c). The overall VR_{SAR} was 85%, with $VR_{SAR,amp}$ (all 3 components) and $VR_{SAR,pha}$ (only horizontal components) coming out to 97 and 98%, respectively. The poorer fitting in the north–south component may be due to the relatively smaller observed north–south component amplitudes being difficult to model, particularly if the deformation/GNSS station location is above the modeled fault, where it is more sensitive to the dip angle of the faults.

For the tsunami stations, the overall $VR_{tsunami}$ was 8%, with the best fits to the Fukui and Kanazawa WG stations. Fits to stations not used in the inversion were much poorer (Fig. S18). When all tsunami stations were used in the three-dataset inversion (with optimal weightings readjusted), the overall $VR_{tsunami}$ increased to 27% (Fig. S10). This is expected as the weighting of the tsunami data set went up to 0.4. When conducting a tsunami-only inversion (Fig. S11) using the same stations, as shown in Fig. 3, $VR_{tsunami}$ went up to ~70%. When all 14 tsunami stations were used in the tsunami-only inversion (Fig. S12), the $VR_{tsunami}$ dropped to ~38%. This is expected as more observations are being fit, highlighting the tradeoff between the number of stations and waveform fitting. While wave heights were generally well-reproduced, they were slightly underestimated, likely caused by station relocations to deeper offshore waters due to bathymetric resolution constraints near shorelines. Moreover, stations located in harbors tend to experience significant wave amplification (Synolakis 2003; Lynett et al. 2012). In addition, some stations had phase shifts that greatly dropped their VR value (e.g., Mikuni). Finally, the static inversions failed to replicate the subsidence signals observed at the Toyama Bay tide gauge station before the main tsunami wave's arrival.

4.2 Adjoint inversion

Our adjoint inversion captured the general area of significant uplift toward the northeast of the Noto Peninsula (Fig. 4a). In addition, an area of similar amplitude in subsidence was identified southeast of the peninsula. The IWE used in our inversion generally reproduces the waveforms well (Fig. 5), achieving an overall VR of ~68%. Notably, the subsidence signals preceding the main tsunami wave at stations in Toyama Bay were accurately captured. Compared to the static result using only tsunami stations (Fig. 4b), both approaches modeled uplift on the western and eastern coasts of the Peninsula. Subsidence was also modeled on the northern and southern coasts. Both also captured further offshore uplifts. However, the further offshore subsidence was not imaged by the adjoint method. This lack of subsidence was also seen in our adjoint inversion test that used the outputted tsunami-only static inversion waveforms as inputs (Fig. S20). It is worth noting that the static inversion result (Fig. 4b) did not image the subsidence on the southeastern coast

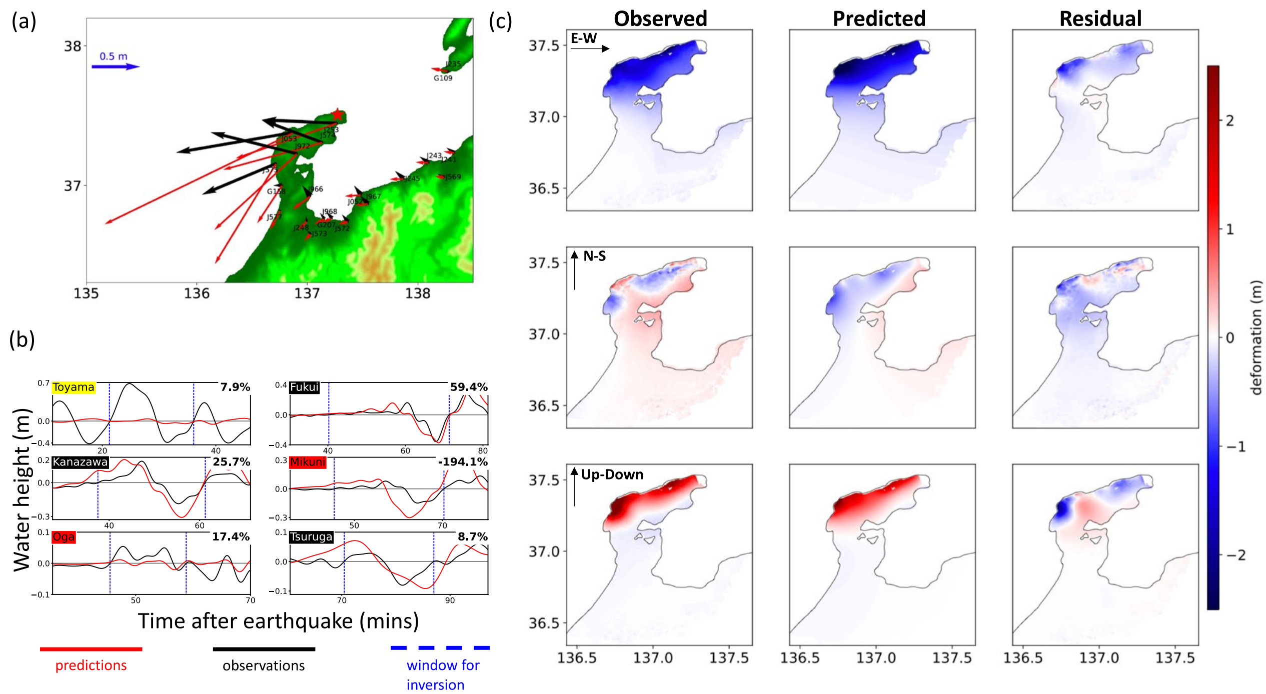

Fig. 3 Model fitting to the data sets used in the joint inversion. **a** Fitting to the GNSS data. Black and red arrows correspond to observations and predictions, respectively. **b** Fitting to the tsunami data. We have indicated the specific VR values for each station in the top-right corner of each plot. Fitting to the stations not used in the inversion is shown in Figure S18. **c** Fitting to the SAR-derived deformation data. The top, middle, and bottom panels correspond to the deformation data's east–west, north–south, and up–down components. Black arrows indicate the positive direction for each component

seen in the adjoint inversion. This may be due to the use of different stations or the impact of coarser bathymetry. Although both methods showed similarities in the locations and types of deformation, the adjoint method produced significantly lower amplitudes. This discrepancy may result from amplitude distortions caused by TRI close to shore, leading to sharp transitions from uplift to subsidence not being fully captured. Moreover, much of the tsunami source's energy remained trapped on the coast, preventing distant stations from receiving the stronger deformation signals during each iteration's forward simulation. As a result, the IWE was likely underestimated. Given that the largest azimuthal gap of the stations we used was ~181°, poor azimuthal coverage, as well as low station density, could also be the reason.

Furthermore, the IWE highlighted significant seafloor disturbances in some areas (circled in Fig. 4a), which were not evident in the deformations from the static inversion. These findings indicate that a static inversion may only partially capture the observations from geodetic and tsunami instruments. Since the adjoint inversion can directly image the tsunami source, signals of significant uplift may sometimes be observed further from the mainshock, possibly representing non-seismic water elevation changes or artifacts from the TRI method due to tsunami wave reflections off the coastline (An and Meng 2017; Zhou et al. 2019). The TRI method works by reversing observed waveforms in time and back-propagating them using station locations as point sources. Since tsunami waves reflect off coastlines, if the time window used in the inversion overlaps with the time at which reflection occurs, this can distort the backpropagation, leading to zones of deformation near the coast in the IWE. The risk of this overlap is higher when coastal gauges are used, because the reflected wave will arrive right after the main tsunami wave's arrival. In a previous synthetic test that used ocean bottom pressure gauges (OBPGs; Xie et al. 2023), the effect of coastal artifacts on the inversion result was minimal, since the stations were in much deeper water.

To further demonstrate the concept of a coastal artifact, we ran a synthetic test of the adjoint inversion's ability to resolve the seafloor deformation caused by a single rectangular subfault near the mainshock's epicenter (Fig. S21a, b). Comparing the inversion result (Fig. S21c, d) with the source's IWE, we notice that the largest area of significant uplift is located towards the northeast of the peninsula, coinciding with the location of uplift in the synthetic source, albeit with an underestimation of the amplitude. We also see significant uplift and subsidence

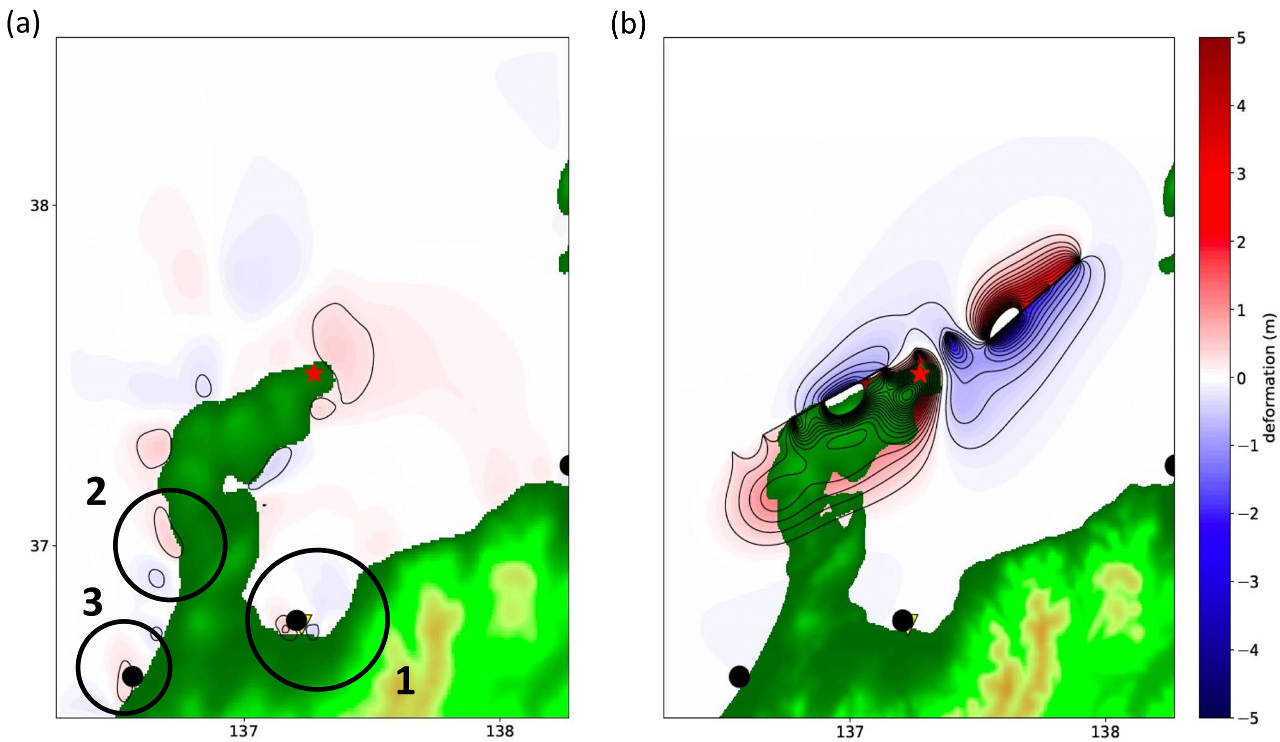

Fig. 4 Comparison between adjoint and static inversion results. **a** Vertical seafloor deformation (IWE) obtained using the adjoint inversion of stations highlighted in Fig. 5. Areas highlighted with thick solid black circles and numbers indicate the areas used for analysis in Fig. 5. **b** Vertical seafloor deformation obtained using a static inversion of only tsunami data. The slip model associated with this result is shown in Fig. S11

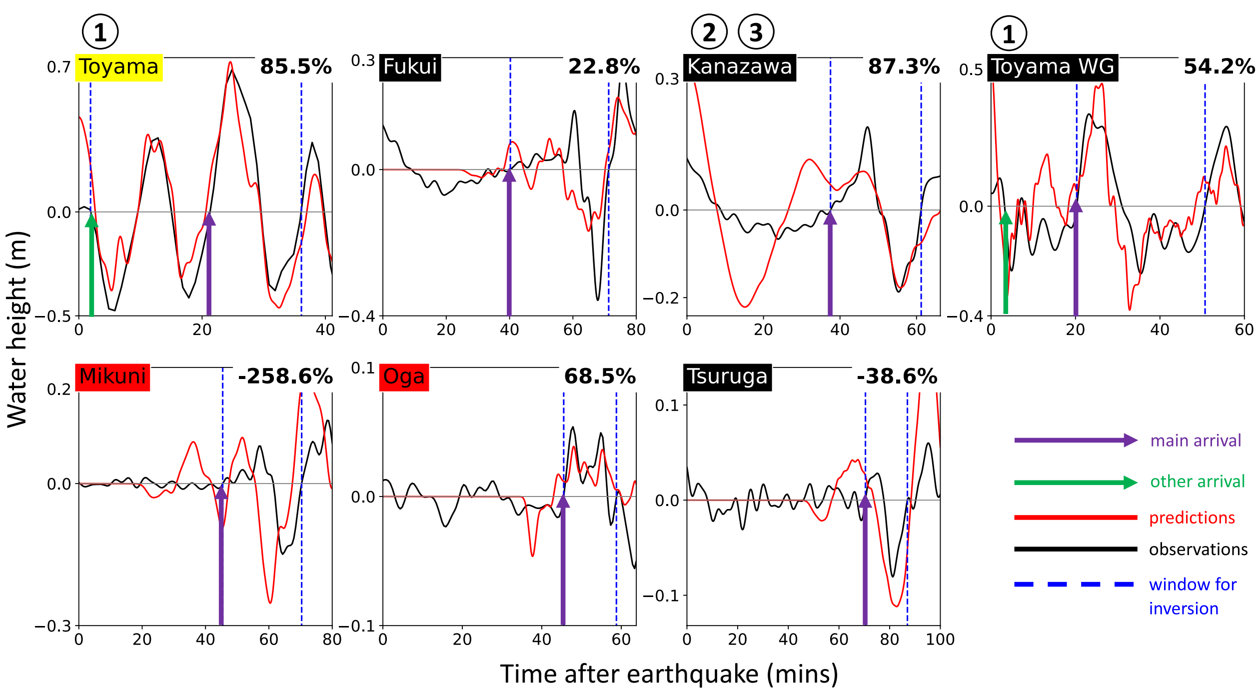

Fig. 5 Model fitting to the tsunami stations used in the adjoint inversion. Waveform fitting of the IWE from Fig. 4a. Stations examined for non-earthquake-induced arrivals are marked with a circle corresponding to the closest area from Fig. 4a. Purple and green arrows indicate the arrival of earthquake and non-earthquake-induced tsunami waves, respectively. Fits to the stations not used in the inversion are shown in Fig. S19

signals near the coastline on the western side of the peninsula, where there should be none. These false seafloor deformation signals are the coastal artifacts. These could be due to the geometry of the bathymetry. The western side has a more gently sloping profile (Fig. S22), with a shallower ocean bottom extending further offshore compared to the steeper and deeper eastern side. This shallower water leads to more nonlinear interactions of arriving waves with the ocean bottom, causing more artifacts in the TRI initial guess.

To differentiate between coastal artifacts, coseismic deformation, and other phenomena in our result, we analyze the highlighted areas in Fig. 4, searching for evidence of uplift or subsidence before the main tsunami's arrival at the nearest stations. In cases where no nearby stations exist, these areas are considered potential landslide zones.

For Area 1, the nearest instruments are the Toyama WG and TG stations. Analysis of their waveforms reveals a subsidence signal indicated by green arrows in Fig. 5, followed by some uplift occurring approximately 20 min after the earthquake, before the main tsunami wave's arrival (purple arrow in Fig. 5). This observation eliminates the possibility of a coastal artifact. In addition, the seafloor deformation mapped in the static inversion (Fig. 2b) does not indicate any significant changes in Toyama Bay, thereby excluding deformation caused by the mainshock. Forward modeling by Masuda et al. (2024a) suggests that a landslide on a 20° slope could account for the observations at the TG station. Mulia et al. (2024) also imaged a signal of similar amplitude to our result in Toyama Bay using the tsunami backpropagated travel-time technique (Mulia and Asano, 2016; Hayashi et al., 2011). The adjoint method has been shown to detect coseismic landslides using synthetic data (Xie et al. 2023). To demonstrate this ability closer to shore, we ran a synthetic test using the synthetic landslide sources tested in Masuda et al. (2024b) and found that the adjoint method captures the location of the maximum energy of the landslide signal accurately (Fig. S23). In addition, the single subfault synthetic test (Fig. S21) does not show a large coastal artifact in Toyama Bay, so the contribution of wave reflections from that area is likely minimal. Landslide evidence is supported by reports and field surveys from the Japanese Coast Guard (2024a, b), pointing to the likelihood that the adjoint inversion successfully imaged a landslide in Toyama Bay. This instance marks the first successful imaging of a landslide with the adjoint method using observed tsunami recordings.

For Area 2, the uplift corresponds with areas of coseismic deformation identified in the static inversion. No signals were detected at the closest station, Kanazawa WG, before the arrival of the first tsunami wave (around 40 min), suggesting that the uplift is part of the coseismic deformation field. However, the single sub-fault synthetic test shows significant uplift and subsidence in that area, so it is difficult to say whether Area 2 corresponds to a real deformation signal or a coastal artifact.

For Area 3, the static inversion results show no coseismic deformation at the same location, and observations at the Kanazawa WG do not exhibit any significant uplift or subsidence after the earthquake origin time and before the first tsunami wave's arrival. In addition, the single subfault synthetic test shows significant uplift and subsidence in that area. Therefore, Area 3 is categorized as a coastal artifact.

As a sanity check, we ran the adjoint inversion using all 14 stations (Fig. S24), and we found the location of the possible artifacts remained mostly the same. We discuss the new artifacts near Naoetsu in Text S3.

5 Discussion

Compared to other researchers, such as Fujii and Satake (2024) and Mizutani et al. (2024), our static inversion results demonstrated moderate performance. Qualitative inspection of Fujii and Satake's (2024) results shows that they reproduced tsunami and GNSS observations at most stations, albeit with a consistent underestimation of amplitudes. Mizutani et al. (2024) reported VR values of 76.2% for the tsunami data and 94.1% for the GNSS data. Ma et al. (2024) achieved great fits to their GNSS and SAR-derived observations, though they used a different set of GNSS stations than we did. However, none of these studies have tried to reconcile a combination of tsunami, SAR-derived deformation, and GNSS data. Our obtained VR values are in the moderate range of VR fitting. Factors lowering the VR values may be the dip angle of the fault geometry as well as the limitation of bathymetry resolution for the tsunami stations. In addition, attempting to reconcile three data sets of different types (water height and geodetic) is more challenging than reconciling two. Furthermore, no authors were able to model the Toyama Bay tide gauge station's initial subsidence signal accurately using the adjoint inversion method.

Our adjoint inversion's VR was generally greater than most of our static inversion methods, achieving a $VR_{tsunami}$ of ~68%. This VR is higher than that of Xie et al. (2023)'s application of the method to the 2016 M_w 6.9 Fukushima earthquake, which also occurred close (<35 km) to shore and was susceptible to artifacts. While Masuda et al. (2024a) showed through forward modeling that a landslide could explain the observations at Toyama Bay, none have shown this through an inversion. Despite the presence of coastal artifacts, our analysis is still useful, since the fitting to the stations in Toyama Bay improved compared to the static case (from ~4 to ~54% and ~8 to

~86% for the WG and TG, respectively). In contrast, the static inversion method and results from other authors primarily replicated the main tsunami signal.

One limitation of our results is the adjoint method's tendency to underestimate the amplitude of seafloor deformation. In addition, the accuracy of the adjoint inversion depends on the initial guess, which is influenced by the density of the station network, azimuthal coverage, and the coastal proximity of the tsunami source. While our adjoint approach underestimates the IWE amplitude, it remains valuable for identifying the general location of major deformation sources, particularly when combined with the coastal artifact test in Fig. S21. However, the current formulation of the adjoint method is best suited for capturing seafloor disturbance amplitudes in deeper water. In addition, the linear shallow water equations do not account for nonlinear interactions between tsunami waves and the ocean bottom, which may impact accuracy. Future improvements should integrate nonlinear effects in forward simulations, as in the approach presented by Takagawa et al. (2024), which may be more suitable for near-shore applications.

Our analysis of the highlighted areas in Fig. 4a shows the adjoint method's capacity to detect non-seismic tsunami sources, such as landslides, which enhance waveform fitting and are crucial for issuing accurate tsunami warnings and evacuation orders. Notably, in this case, waves induced by landslides preceded the predicted main tsunami wave (Japanese Coast Guard 2024a, b), potentially affecting residents' ability to evacuate promptly. Given that the stations used were near-shore and may not offer sufficient warning time for the main tsunami wave, this emphasizes the importance of a dense network of OBPGs, akin to the Seafloor Observation Network for Earthquakes and Tsunamis along the Japan Trench (S-net), for the Sea of Japan. In addition, earthquakes occurring on hazardous thrust faults located further offshore at the Amur–Okhotsk plate boundary (MLIT 2014; Sato et al. 2020) could trigger landslides that amplify tsunami wave run-up, thus necessitating a dense OBPG network that provides crucial lead time in a warning system.

6 Conclusion

We conducted a comprehensive analysis of the 2024 M_w 7.5 Noto Peninsula earthquake and its resulting tsunami using static and adjoint inversions of geodetic and tsunami data sets. The adjoint method, which uses time-reversal imaging, enables direct imaging of the tsunami source without assuming a predefined earthquake fault geometry. This makes it particularly effective for detecting non-seismic seafloor disturbances, such as landslides. Both inversion methods consistently identified slip and crustal deformation off the northeastern coast. The adjoint-state method achieved better fits at select stations and, despite the limitations in near-field station density, coverage, and amplitude distortions, successfully imaged a landslide in Toyama Bay. This marks the first instance of resolving a landslide using observed water level data. Our findings highlight the potential of the adjoint method to enhance tsunami warning systems by detecting non-seismic tsunami sources. While the current formulation is best suited for deep-water scenarios, incorporating nonlinear effects of shallow-water wave propagation could improve amplitude resolution near the shore.

Abbreviations

GNSS	Global Navigation Satellite System
JMA	Japanese Meteorological Agency
USGS	United States Geological Survey
M JMA	Modified Japan Meteorological Agency magnitude
MLIT	Ministry of Land, Infrastructure, Transport, and Tourism
JSPJ	Japan Sea Earthquake and Tsunami Project
PCOMCOT	Parallel Cornell Multi-grid Coupled Tsunami Model
GEBCO	General Bathymetric Chart of the Oceans
IOC	International Oceanographic Commission
WG	Wave gauge
TG	Tide gauge
SAR	Synthetic Aperture Radar
NOWPHAS	Nationwide Ocean Wave information network for Ports and HArbourS
VR	Variance reduction
NGL	Nevada Geodetic Laboratory
GSI	Geospatial Information Authority of Japan
IWE	Initial water elevation
TRI	Time-reversal imaging

Supplementary Information

The online version contains supplementary material available at https://doi.org/10.1186/s40623-025-02197-7.

Additional file 1.

Additional file 2.

Acknowledgements

This work used computational and storage services associated with the Hoffman2 Cluster, which is operated by the UCLA Office of Advanced Research Computing's Research Technology Group.

Author contributions

S.M.: investigation, visualization, methodology, data curation/acquisition, validation, and writing (first draft, review, and editing). L.M.: investigation, writing (review and editing), and funding. T.C.H: data acquisition, processing, and writing (review and editing). C.A.: methodology and writing (review and editing). L.X.: data acquisition and writing (review and editing).

Funding

This work is supported by the National Science Foundation's CAREER Grant EAR-1848486.

Availability of data and materials

The General Bathymetric Chart of the Oceans (2023) provided our 15- and 30-arc-sec bathymetry data (www.gebco.net). The M700 series, 6-arcsec data (Figure S2) was obtained from Kyoto University. The adjoint inversion code is available for download from https://doi.org/https://doi.org/10.5281/zenodo.8394585 (Xie 2023). Data from tide gauge stations are available for downloading from the IOC and GSI websites (https://www.ioc-sealevelmonitoring.org/, https://www.gsi.go.jp/kanshi/tide_furnish.html). Raw wave gauge data were digitized using the software PlotDigitizer (2024, https://plotdigitizer.com/) from the Port and Harbor Bureau's NOWPHAS website (https://www.mlit.go.jp/kowan/nowphas/). The GNSS data were obtained from the Nevada Geodetic Library (NGL, 2024) website. The SAR-derived deformation data were obtained from Ma et al. (2024). Figures were generated with assistance from the Clawpack finite volume modeling software (Clawpack Development Team 2024) and Matplotlib (Hunter ., 2007). The 3D-faults software from Mildon et al. (2016) used to coarsen the fault geometry can be found at https://github.com/ZoeMildon/3D-faults.git.

Declarations

Ethics approval and consent to participate
Not applicable.

Consent for publication
Not applicable.

Competing interests
The authors declare that they have no competing interests.

Author details
[1]Department of Earth, Planetary and Space Sciences, University of California Los Angeles, Los Angeles, CA, USA. [2]Disaster Prevention Research Institute, Kyoto University, Kyoto, Japan. [3]Key Laboratory of Hydrodynamics (Ministry of Education), School of Naval Architecture, Ocean and Civil Engineering, Shanghai Jiao Tong University, Shanghai, China.

Received: 28 October 2024 Accepted: 23 April 2025
Published online: 06 August 2025

References
Akaike H (1980) Likelihood and the Bayes procedure. Trabajos Estad Y Invest Oper 31:143–166
Amezawa Y, Hiramatsu Y, Miyakawa A, Imanishi K, Otsubo M (2023) Long-living earthquake swarm and intermittent seismicity in the northeastern tip of the Noto Peninsula, Japan. Geophys Res Lett 50:e2022GL102670. https://doi.org/10.1029/2022GL102670
An C, Meng L (2017) Time reversal imaging of the 2015 Illapel tsunami source. Geophys Res Lett 44:1732–1739. https://doi.org/10.1002/2016GL071304
An C, Sepúlveda I, Liu PL-F (2014) Tsunami source and its validation of the 2014 Iquique, Chile Earthquake. Geophys Res Lett 41:3988–3994. https://doi.org/10.1002/2014gl060567
Bertiger W, Bar-Sever Y, Dorsey A, Haines B, Harvey N, Hemberger D, Heflin M, Lu W, Miller M, Moore AW, Murphy D, Ries P, Romans L, Sibois A, Sibthorpe A, Szilagyi B, Vallisneri M, Willis P (2020) Gipsyx/rtgx, a new tool set for space geodetic operations and research. Adv Space Res 66(3):469–489. https://doi.org/10.1016/j.asr.2020.04.015
Byun S-S, Kim KO (2021) A study on the impacts of the 1741 tsunami recorded in the annals of Joseon Dynasty. J Korean Soc Coast Ocean Eng 33(1):30–37. https://doi.org/10.9765/kscoe.2021.33.1.30. (**in Korean**)
Clawpack Development Team (2024) Clawpack Version 5.10.0, http://www.clawpack.org, https://doi.org/10.5281/zenodo.10896214
Fujii Y, Satake K (2024) Slip distribution of the 2024 Noto Peninsula earthquake (MJMA 7.6) estimated from tsunami waveforms and GNSS data. Earth Planets Space 76:44. https://doi.org/10.1186/s40623-024-01991-z
General Bathymetric Chart of the Oceans. (2023). Gridded bathymetry data. General Bathymetric Chart of the Oceans. Gebco. www.gebco.net
Hayashi, Y., Tsushima, H., Hirata, K. et al. Tsunami source area of the 2011 off the Pacific coast of Tohoku Earthquake determined from tsunami arrival times at offshore observation stations. Earth Planets and Space 63, 54 (2011). https://doi.org/10.5047/eps.2011.06.042
Hossen MJ, Cummins PR, Roberts SG et al (2015) Time reversal imaging of the Tsunami Source. Pure Appl Geophys 172:969–984. https://doi.org/10.1007/s00024-014-1014-5
Hunter JD (2007) Matplotlib: a 2D graphics environment. Comput Sci Eng 9(3):90–95. https://doi.org/10.1109/MCSE.2007.55
Ishikawa Prefectural Government (2024) Human and building damage caused by the 2020 Noto Peninsula Earthquake. Retrieved from https://www.pref.ishikawa.lg.jp/saigai/documents/higaihou_144_0709_1400.pdf [in Japanese]
Japan Coast Guard (JCG) (2024b) Confirmation of slope failure's trace in the sea bottom of Toyama Bay (second report). https://www.kaiho.mlit.go.jp/info/kouhou/r6/k240311_2/k240311_2.pdf (in Japanese, translated title)
Japanese Coast Guard (2024a) Traces of Slope Failure Confirmed on the Seafloor Toyama Bay. Retrieved from https://www.kaiho.mlit.go.jp/info/kouhou/r6/k240124/k240124.pdf and https://www.kaiho.mlit.go.jp/info/kouhou/r6/k240311_2/k240311_2.pdf (in Japanese)
Kato A (2024) Implications of fault-valve behavior from immediate aftershocks following the 2023 Mj6.5 earthquake beneath the Noto Peninsula, central Japan. Geophys Res Lett 51:e2023GL106444. https://doi.org/10.1029/2023GL106444
Kubota T, Kubo H, Yoshida K, Chikasada NY, Suzuki W, Nakamura T, Tsushima H (2021) Improving the constraint on the Mw7.1 2016 off-Fukushima shallow normal-faulting earthquake with the high azimuthal coverage tsunami data from the S-net wide and dense network: Implication for the stress regime in the Tohoku overriding plate. J Geophys Res Solid Earth 126:e2021JB022223. https://doi.org/10.1029/2021JB022223
Lawson CL, Hanson RJ (1995) Solving least squares problems. Society for Industrial and Applied Mathematics, Philadelphia
Liu PL-F, Woo S-B, Cho Y-S (1998) Computer programs for tsunami propagation and inundation. Cornell University, Ithaca
Liu J, Hu J, Li Z, Ma Z, Shi J, Xu W, Sun Q (2022) Three-dimensional surface displacements of the 8 January 2022 Mw 6.7 Menyuan earthquake, China from Sentinel-1 and AlOS-2 SAR observations. Remote Sens 14:1404. https://doi.org/10.3390/rs14061404
Lynett PJ, Borrero JC, Weiss R, Son S, Greer D, Renteria W (2012) Observations and modeling of tsunami-induced currents in ports and harbors. Earth Planet Sci Lett 327–328:68–74. https://doi.org/10.1016/j.epsl.2012.02.002
Ma Z et al (2024) Slow rupture in a fluid-rich fault zone initiated the 2024 Mw 7.5 Noto earthquake. Science 385:866–871. https://doi.org/10.1126/science.ado5143
Masuda H, Sugawara D, Cheng A-C, Suppasri A, Shigihara Y, Kure S, Imamura F (2024a) Modeling the 2024 Noto Peninsula earthquake tsunami: Implications for tsunami sources in the eastern margin of the Japan Sea. Geosci Lett 11:29. https://doi.org/10.1186/s40562-024-00344-8
Masuda H, Sugawara D, Cheng A-C, Suppasri A, Shigihara Y, Kure S, Imamura F (2024b) Modeling the 2024 Noto Peninsula earthquake tsunami: implications for tsunami sources in the eastern margin of the Japan Sea. Res Square. https://doi.org/10.21203/rs.3.rs-3945364/v1
Mildon ZK, Toda S, Faure Walker JP, Roberts GP (2016) Evaluating models of Coulomb stress transfer- is variable fault geometry important? Geophys Res Lett 43:12407–12414. https://doi.org/10.1002/2016GL071128
Mizutani A, Adriano B, Mas E et al (2024) Fault model of the 2024 Noto Peninsula Earthquake Based on Aftershock, Tsunami, and GNSS Data. Res Square. https://doi.org/10.21203/rs.3.rs-4167995/v1
MLIT (2014) Investigation for large earthquakes occurring in the Sea of Japan. https://www.mlit.go.jp/river/shinngikai_blog/daikibojishinchousa/
Mulia IE, Ishibe T, Satake K et al (2020) Regional probabilistic tsunami hazard assessment associated with active faults along the eastern margin of the Sea of Japan. Earth Planets Space 72:123. https://doi.org/10.1186/s40623-020-01256-5
Mulia IE, Heidarzadeh M, Gusman A, Satake K, Fujii Y, Sujatmiko KA, Meilano I, Windupranata W (2024) Compounding impacts of the earthquake and submarine landslide on the Toyama Bay tsunami during the January 2024 Noto Peninsula event. Ocean Engineering 310(1):118698. https://doi.org/10.1016/j.oceaneng.2024.118698
Murotani S, Satake K, Ishibe T et al (2022) Reexamination of tsunami source models for the twentieth century earthquakes off Hokkaido and Tohoku along the eastern margin of the Sea of Japan. Earth Planets Space 74:52. https://doi.org/10.1186/s40623-022-01607-4
Mulia, I. E., and T. Asano (2016), Initial tsunami source estimation by inversion with an intelligent selection of model parameters and time delays, Journal of Geophysical Research: Oceans, 121, 441–456. https://doi.org/10.1002/2015JC010877
National Geophysical Data Center / World Data Service: NCEI/WDS Global Historical Tsunami Database. NOAA National Centers for Environmental Information. https://doi.org/10.7289/V5PN93H7. Accessed April 11, 2024.

Nevada Geodetic Laboratory (NGL). Damaging M7.5 Earthquake hits (2024) https://geodesy.unr.edu/news_items/20240104/us6000m0xl_forweb.txt. [Dataset]. Accessed January 6, 2024
Nishimura T, Hiramatsu Y, Ohta Y (2023) Episodic transient deformation revealed by the analysis of multiple GNSS networks in the Noto Peninsula, central Japan. Sci Reports 13:8381. https://doi.org/10.1038/s41598-023-35459-z
Okada Y (1985) Surface deformation due to shear and tensile faults in a half-space. Bull Seismol Soc Am 75(4):1135–1154. https://doi.org/10.1785/BSSA0750041135
Plessix R-E (2006) A review of the adjoint-state method for computing the gradient of a functional with geophysical applications. Geophys J Int 167(2):495–503. https://doi.org/10.1111/j.1365-246X.2006.02978.x
PlotDigitizer: Version 4.5; https://plotdigitizer.com/ [Software]
Satake K (2007) Volcanic origin of the 1741 Oshima-Oshima tsunami in the Japan Sea. Earth Planets Space 59:381–390. https://doi.org/10.1186/BF03352698
Satake K, Ishibe T, Murotani S et al (2022) Effects of uncertainty in fault parameters on deterministic tsunami hazard assessment: examples for active faults along the eastern margin of the Sea of Japan. Earth Planets Space 74:36. https://doi.org/10.1186/s40623-022-01594-6
Sato H, Ishiyama T, Hashima A, Kato N, Van-Horne A, Claringbould JS, No T, Ishikawa M, Matsubara M, Koshiya S, Toyoshima T, Kobayashi K, Kosuga M (2020) Development of active fault model. Annual Progress Reports of the Integrated Research Project on Seismic and Tsunami Hazards around the Sea of Japan (FY2019), 209–239 (in Japanese)
Sekiguchi H, Irikura K, Iwata T (2000) Fault Geometry at the Rupture Termination of the 1995 Hyogo-ken Nanbu Earthquake. Bulletin of the Seismological Society of America 90(1):117–133. https://doi.org/10.1785/0119990027
Synolakis CE (2003) Tsunami and seiche. Earthquake engineering handbook, vol 9. CRC Press, Boca Raton, pp 1–9
Takagawa T, Allgeyer S, Cummins P (2024) Adjoint synthesis for trans-oceanic tsunami waveforms and simultaneous inversion of fault geometry and slip distribution. J Geophys Res Solid Earth 129:e2024JB028750. https://doi.org/10.1029/2024JB028750
Tarantola A (1986) A strategy for nonlinear elastic inversion of seismic reflection data. Geophysics 51(10):1893–1903. https://doi.org/10.1190/1.1442046
Tromp J, Tape C, Liu Q (2004) Seismic tomography, adjoint methods, time reversal and banana-doughnut kernels. Geophys J Int 160(1):195–216. https://doi.org/10.1111/j.1365-246X.2004.02453.x
U.S. Geological Survey (n.d.) Google Earth™/KML Files: Earthquake Hazards Program. U.S. Department of the Interior. Retrieved from https://www.usgs.gov/programs/earthquake-hazards/google-earthtmkml-files
Wang X, Liu PLF (2006) An analysis of 2004 Sumatra earthquake fault plane mechanisms and Indian Ocean tsunami. J Hydraul Res 44(2):147–154. https://doi.org/10.1080/00221686.2006.9521671
Woessner J, Farahani RJ (2020) Tsunami inundation hazard across Japan. Int J Disaster Risk Reduct 49:101654. https://doi.org/10.1016/j.ijdrr.2020.101654
Xie Y, Mohanna S, Meng L, Zhou T, Ho T-C (2023) Adjoint inversion of near-field pressure gauge recordings for rapid and accurate tsunami source characterization. Earth Space Sci 10:e2023EA003086. https://doi.org/10.1029/2023EA003086
Xie Y (2023) Tsunami adjoint inversion [Software]. Zenodo. https://doi.org/10.5281/zenodo.8394585
Yoshida K, Uno M, Matsuzawa T, Yukutake Y, Mukuhira Y, Sato H, Yoshida T (2023) Upward earthquake swarm migration in the northeastern Noto Peninsula, Japan, initiated from a deep ring-shaped cluster: Possibility of fluid leakage from a hidden magma system. J Geophys Res Solid Earth 128:e2022JB026047. https://doi.org/10.1029/2022JB026047
Yuhi M, Umeda S, Arita M, Ninomiya J, Gokon H, Arikawa T et al (2024) Post-event survey of the 2024 Noto Peninsula earthquake tsunami in Japan. Coast Eng J 66:405–418. https://doi.org/10.1080/21664250.2024.2368955
Zhou T, Meng L, Xie Y, Han J (2019) An adjoint-state full-waveform tsunami source inversion method and its application to the 2014 Chile-Iquique tsunami event. J Geophys Res Solid Earth 124:6737–6750. https://doi.org/10.1029/2018JB016678
Zhu Yf, An C, Wang T et al (2021) Time-dependent tsunami source following the 2018 Anak Krakatau Volcano Eruption inferred from nearby tsunami recordings. China Ocean Eng 35:145–152. https://doi.org/10.1007/s13344-021-0013-4

Publisher's Note